RANS Solutions Using High Order Discontinuous Galerkin Methods

Ngoc Cuong Nguyen*, Per-Olof Persson† and Jaime Peraire‡
Massachusetts Institute of Technology, Cambridge, MA 02139, U.S.A.

We present a practical approach for the numerical solution of the Reynolds averaged Navier-Stokes (RANS) equations using high-order discontinuous Galerkin methods. Turbulence is modeled by the Spalart-Allmaras (SA) one-equation model. We introduce an artificial viscosity model for SA equation which is aimed at accommodating high-order RANS approximations on grids which would otherwise be too coarse. Generally, the model term is only active at the edge of the boundary layer, where the grid resolution is insufficient to capture the abrupt change in curvature required for the eddy viscosity profile to match its free-stream value. Furthermore, the amount of viscosity required decreases with the grid resolution and vanishes when the resolution is sufficiently high. For transonic computations, an additional shock-capturing artificial viscosity model term is required. Numerical predictions for turbulent flows past a flat plate and a NACA 0012 airfoil are presented via comparison with the experimental measurements. In the flat plate case, grid refinement studies are performed in order to assess the convergence properties and demonstrate the effectiveness of high-order approximations.

I. Introduction

A variety of real-life problems in computational fluid dynamics (CFD) requires accurate modeling and simulation of complex turbulent flows. However, it is well known that the cost of simulating such flows even for modest Reynolds numbers is extremely high. The direct numerical simulation of turbulent flows with reasonably large Reynolds numbers simply exceeds the existing capabilities of today's computers. A popular approach to overcome this problem is to solve the Reynolds-averaged Navier-Stokes (RANS) supplemented with a turbulence model. The numerical solution of the RANS equations with a turbulence closure model has been a subject of extensive research.[13] Although known as the least demanding of all turbulence simulation methods, RANS solutions still demand significant computational resources especially for complex flows involving boundary layers and separation. Systems of several million degrees of freedom are common; unfortunately grid convergence, and hence reliable accuracy, is not always attained. In this paper, we investigate the use of high-order approximations as a means of reducing the computational costs required to obtain grid converged RANS solutions.

High-order methods applied to non-linear problems tend to become unstable when the approximating space is inadequate to resolve the main features of the true solution. Unresolved boundary layers produce Gibbs oscillations which, in the presence of non-linearly, often lead to solution blow-up. RANS solutions contain a large range of scales which make it difficult to know a-priori the grid requirements, specially when small length scale features occur away from the walls. In practice, it is often necessary to supplement the turbulence model equations with some form of stabilization to prevent the eddy viscosity from becoming negative at the unresolved layer. In this paper, we develop an artificial viscosity term for the turbulence model equation which is aimed at stabilizing the RANS solutions in situations where the grid resolution is insufficient. We consider the Spalart-Allmaras (SA) one-equation model[11] but we expect that the approach

*Postdoctoral Associate, Department of Aeronautics and Astronautics, MIT, 77 Massachusetts Avenue 37-435, Cambridge, MA 02139. E-mail: cuongng@mit.edu.
†Instructor, Department of Mathematics, MIT, 77 Massachusetts Avenue 2-363A, Cambridge, MA 02139. E-mail: persson@mit.edu. AIAA Member.
‡Professor, Department of Aeronautics and Astronautics, MIT, 77 Massachusetts Avenue 37-451, Cambridge, MA 02139. E-mail: peraire@mit.edu. AIAA Associate Fellow.

described can be usefully applied to other turbulence models. In the SA model an additional equation for a modified eddy viscosity variable is solved. A peculiarity of the SA model is the the abrupt change in curvature that the profile of the eddy viscosity exhibits at the edge of the boundary layer. This is illustrated in figure 1 which shows normalized values of the modified eddy viscosity variable versus the distance to the wall. We note the abrupt curvature change at the edge of the boundary layer $y/\delta^* \approx 8.5$ just before leveling off to the free-stream value. Simple dimensional analysis reveals that the thickness of this transition region scales like the laminar viscosity, and therefore, it numerical approximation requires an unrealistic level of resolution.

The main purpose of the added artificial viscosity term is to smooth out this transition layer to a thickness which can be resolved by the available grid. Consequently, the amount of artificial viscosity required decreases when the resolution is increased and eventually vanishes when the grid resolution is sufficient. It is worth noting that even thought the eddy viscosity profile is modified by the added artificial viscosity, its effect on the flow solution is minimal since the values of the eddy viscosity in that region are very small.

The spatial discretization of the RANS equations with the addition of the SA model is accomplished using high-order discontinuous Galerkin methods. Discontinuous Galerkin (DG) methods have gained increased popularity over recent years for the solution of the Euler and Navier-Stokes equations of gas dynamics. The ability to obtain very accurate spatial discretizations on arbitrary unstructured meshes renders DG methods very attractive. Bassi et. al[3] first used the DG methods for the numerical solution of compressible RANS and $k-\omega$ turbulence model equations. The results reported therein have demonstrated the effectiveness of the DG methods for obtaining accurate solutions, but with the consideration of spatial discretizations up to order $p = 2$. Our goal here is to present RANS solutions using high-order polynomial approximations in the range $p = 3 - 4$.

For many applications of interest involving the RANS equations at high Reynolds numbers, the time and length scales are such that implicit discretization turns out to be a requirement. Here, we use a Backward Difference Formula (BDF) time integration method and solve a non-linear system of equations using Newton's method with a block-ILU/multigrid preconditioned GMRES solver for the each linear iteration (see [9]).

The discretization of second order derivatives is not straightforward with DG methods. A number of methods have been proposed to extend DG methods to elliptic problems, each of them having some merits and drawbacks. In this paper, we use the Compact Discontinuous Galerkin (CDG) method.[7] The CDG method is compact and produces a sparser connectivity matrix than the alternative methods such as the Local Discontinuous Galerkin (LDG) method[4] and BR2 method.[2] This results in lower storage requirements and higher computational performance. This is particularly advantageous when an implicit solution method is required.

To demonstrate the soundness of the proposed approach, we present numerical predictions for transonic turbulent flows past a flat plate and a NACA 0012 airfoil, and compare the results with experimental measurements. In addition, for the flat plate case, we present some grid refinement studies in order to assess the convergence properties of the method.

II. Governing Equations

A. RANS Formulation

We consider the compressible time-averaged Navier-Stokes equations

$$\frac{\partial \rho}{\partial t} + \frac{\partial \rho u_j}{\partial x_j} = 0 \tag{1}$$

$$\frac{\partial}{\partial t}(\rho u_i) + \frac{\partial}{\partial x_j}(\rho u_i u_j) + \frac{\partial p}{\partial x_i} - \frac{\partial \tau_{ji}}{\partial x_j} = 0 \tag{2}$$

$$\frac{\partial}{\partial t}(\rho E) + \frac{\partial}{\partial x_j}(u_j(\rho E + p)) - \frac{\partial}{\partial x_j}(u_i \tau_{ji}) + \frac{\partial q_j}{\partial x_j} = 0 \tag{3}$$

$$p = (\gamma - 1)\rho(E - u_k^2/2) \tag{4}$$

$$q_j = -\frac{(\mu + \mu_t)}{Pr}\frac{\partial}{\partial x_j}(E + p/\rho - u_k^2/2) \tag{5}$$

$$\tau_{ij} = (\mu + \mu_t)\left[\frac{\partial u_i}{\partial x_j} + \frac{\partial u_j}{\partial x_i} - \frac{2}{3}\frac{\partial u_k}{\partial x_k}\delta_{ij}\right] \tag{6}$$

where γ, Pr and μ are the ratio of gas specific heats, the molecular Prandtl number and molecular dynamic viscosity. In the above equations, μ_t is the turbulent dynamic, or eddy, viscosity which is determined by the SA one-equation turbulence model.

B. Spalart-Allmaras One-Equation Model

In the SA model,[11] a working variable $\tilde{\nu}$ is introduced to evaluate the turbulent dynamic viscosity and is governed by the transport equation

$$\frac{D\tilde{\nu}}{Dt} = c_{b1}\tilde{S}\tilde{\nu} + \frac{1}{\sigma}\left[\nabla\cdot\left((\nu+\tilde{\nu})\nabla\tilde{\nu}\right) + c_{b2}\left(\nabla\tilde{\nu}\right)^2\right] - c_{w1}f_w\left[\frac{\tilde{\nu}}{d}\right]^2 . \tag{7}$$

The above model equation is written without the trip terms since they are not used here. We therefore assume that the Reynolds numbers are large enough so that the flow over the whole airfoil surface is turbulent. The turbulent dynamic viscosity is then calculated as

$$\mu_t = \rho\nu_t, \qquad \nu_t = \tilde{\nu}f_{v1}, \qquad f_{v1} = \frac{\chi^3}{\chi^3 + c_{v1}^3}, \qquad \chi = \frac{\tilde{\nu}}{\nu} . \tag{8}$$

The production term is expressed as

$$\tilde{S} = S + \frac{\tilde{\nu}}{\kappa^2 d^2}f_{v2} , \tag{9}$$

$$S = \sqrt{2\Omega_{ij}\Omega_{ij}}, \qquad f_{v2} = 1 - \frac{\chi}{1+\chi f_{v1}} . \tag{10}$$

Here $\Omega_{ij} = \frac{1}{2}(\partial u_i/\partial x_j - \partial u_j/\partial x_i)$ is the rotation tensor and d is the distance from the closest wall. The function f_w is given by

$$f_w = g\left[\frac{1+c_{w3}^6}{g^6 + c_{w3}^6}\right]^{1/6} , \tag{11}$$

$$g = r + c_{w2}(r^6 - r), \qquad r = \frac{\tilde{\nu}}{\tilde{S}\kappa^2 d^2} . \tag{12}$$

The closure constants are recommended and use here are $c_{b1} = 0.1355$, $c_{b2} = 0.622$, $c_{v1} = 7.1$, $\sigma = 2/3$, $c_{w1} = (c_{b1}/\kappa^2) + ((1+c_{b2})/\sigma)$, $c_{w2} = 0.3$, $c_{w3} = 2$, $\kappa = 0.41$.

An attractive feature of the SA model from the numerical standpoint is that the resolution required for the new variable $\tilde{\nu}$ near the wall is less than that required to resolve the velocity profile. This is in contrast with other methods such $k-\epsilon$ where the turbulent variables near the wall may require higher resolution than he velocity itself. Consequently, the SA model is numerically well behaved near the wall and allow for reasonable solutions to be obtained on relatively coarse grids especially if higher-order approximations are used (i.e. y^+ for the first node at a distance of $O(10)$.)

At the edge of the boundary layer however, the situation is different. The profile of the eddy viscosity transitions to its free-stream value over a very narrow layer in which the curvature changes sign. Unless properly resolved, this may lead to non-smooth or even negative numerical values for the eddy viscosity variable. This may easily result in sudden instability in the computations. As an illustration, the profiles of $\tilde{\nu}$ in a flat-plate boundary layer are shown in Figure 1(a) for a very fine grid and in Figure 1(b) for a coarser grid. Note that at the edge of the boundary layer ($(y/\delta^* \approx 8.5)$), $\tilde{\nu}$ becomes negative for the coarse grid but transitions smoothly to its free-stream value for the fine mesh. It turns out that the thickness of this transition region is determined by the laminar viscosity and therefore, it is extremely narrow and impractical to resolve in most cases.

Our proposal to treat the above issue is to introduce an artificial viscosity model to the diffusion term of the SA equation (7). The artificial viscosity model aims to stabilize the discretization of the continuous equation (7) in finite dimensional space, which then accommodates high-order approximations of RANS-SA equations on relatively coarse grids. We point out that the regions where the eddy viscosity profile is modified have a minor effect on the overall solution since they generally correspond to regions where the eddy viscosity is very small.

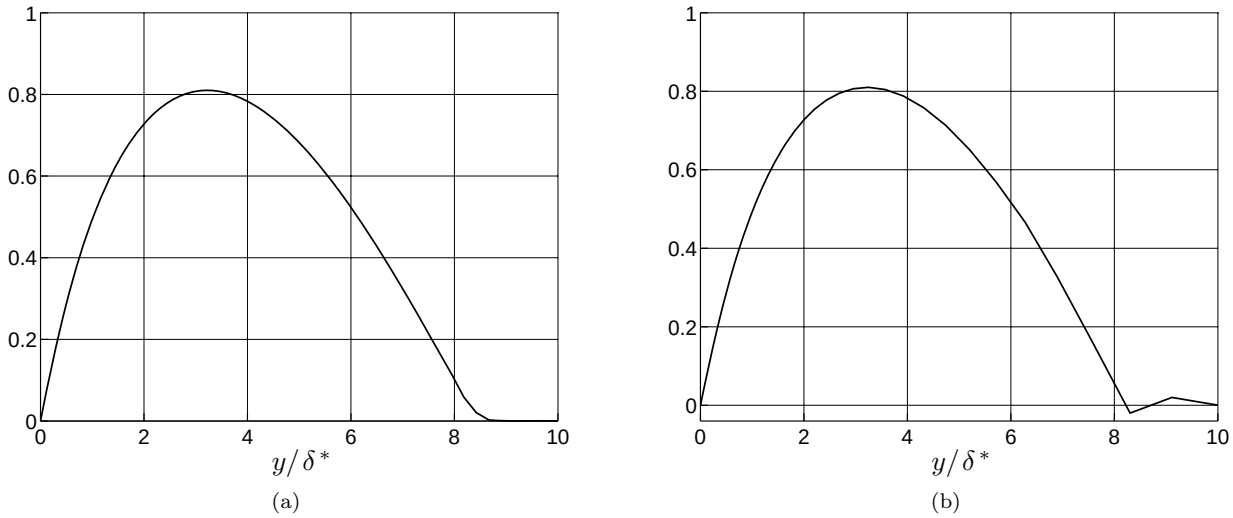

Figure 1. Profiles of the working variable $\tilde{\nu}$ normalized with $0.025U_{\text{edge}}\delta^*$ in a flat-plate boundary layer for: (a) a fine grid and (b) a coarse grid. Here U_{edge} is edge velocity of boundary layer and δ^* is displacement thickness of boundary layer.

III. Proposed Approach for RANS-SA Equations

A. Compact Discontinuous Galerkin Discretization

We write equations (1)-(3) and (7) as a system of partial differential equations in conservative form:

$$\frac{\partial u}{\partial t} + \nabla \cdot F(u, \nabla u) = S(u, \nabla u). \tag{13}$$

To handle the viscous terms, we use the Compact Discontinuous Galerkin method[7] (CDG), where auxiliary variables $q = \nabla u$ are introduced to obtain a system of first-order equations,

$$\frac{\partial u}{\partial t} + \nabla \cdot F(u, q) = S(u, q) \tag{14}$$

$$\nabla u = q. \tag{15}$$

Together with appropriate boundary conditions, this system is discretized in a weak form using a Discontinuous Galerkin technique. The inviscid part of the numerical fluxes is evaluated according to the scheme or Roe[10] and the viscous part is discretized using the CDG method.[7] The resulting system is integrated in time using a BDF method, where in each timestep the nonlinear system of equations is solved by a damped Newton method with a block-ILU/multigrid preconditioned GMRES solver for the linear systems (see [9]). To obtain steady-state solutions, we first use an adaptive time-stepping scheme that increases the timesteps until the solution is sufficiently close to steady-state. Using this solution as initial condition, we then solve for a true stationary solution with a few additional Newton iterations.

B. Stabilizing Model Terms

As discussed above, it is unrealistic to expect the mesh to be fine enough to resolve all the features of the solution. For example, at the edge of the boundary layer very small elements are required to resolve the eddy viscosity $\tilde{\nu}$, but it is not practical to generate such meshes since the location of the boundary layer is unknown a-priori. If such an under-resolved solution is computed using a high-order method, the natural dissipation from the numerical scheme might be insufficient to prevent oscillations, and for nonlinear problems this usually causes the solution to go unstable.

To resolve these issues, we need a stabilization procedure which will allow us to obtain solutions in a reliable way even for coarse meshes. For this, we use the artificial viscosity technique that we proposed in [8]

for the stabilization of shocks. Here, we consider two artificial viscosity model terms: one for the turbulence equation and one for shocks. For each artificial viscosity model term, we identify a key scalar sensor variable. Within in each element, an orthogonal Koornwinder basis[6] for each sensor variable is constructed. The rate of decay of the expansion coefficients is used to estimate deviations in the sensor variable from a smooth function. If the sensor variable is determined to be under-resolved, the corresponding diffusion term is activated with an element piecewise constant value of the viscosity parameter. We note that the artificial viscosity terms are discretized in a manner which is consistent with the differential operator. That is, including both volume as well as inter element fluxes.

Our stabilization consists of two viscous models of the form

$$F_{\text{stab}}(u,q) = \sum_{i=1}^{2} \frac{h}{p} \varepsilon(\psi(s^i(u))) F^i(u,q) \tag{16}$$

which we add to the regular fluxes $F(u,q)$ in (14). Here,

- h and p are element size and the polynomial order of the approximation
- $s^i(u)$ are the *sensor variables*, that is, the variables in which we detect the non-smoothness
- $\psi(s)$ is the *indicator* which, loosely speaking, represents the high frequency content in the sensor variable s. Let $\hat{s}$ represent the nodal variables corresponding to a the discretization of a variable s within an element. We then define the total energy and the energy in the high modes by

$$E = \hat{s}^T M \hat{s} \tag{17}$$

$$E_H = \hat{s}^T M_H \hat{s}. \tag{18}$$

  Here, M is the usual mass matrix for the element, but M_H is the mass matrix using only the high Koornwinder coefficients. Let V be the Koornwinder Vandermonde matrix, with the columns sorted from low to high degree. Define the first n_L modes up to degree $p-1$ as "low", and the remaining n_H modes as "high". Then M_H is defined by the projection $M_H = F_H^T M F_H$ using the filter matrix,

$$F_H = V P_H V^{-1} \text{ with } P_H = \text{diag}(\underbrace{0,\ldots,0}_{n_L},\underbrace{1,\ldots,1}_{n_H}). \tag{19}$$

  The actual indicator is the log of the ratio of the high and total energies,

$$\psi(s) = \log_{10} E_H/E. \tag{20}$$

- $\varepsilon(\psi)$ is the actual piecewise element constant viscosity parameter in the model terms. It varies smoothly between 0 and ε_0, centered at ψ_0 with width $\Delta\psi$:

$$\varepsilon(\psi;\varepsilon_0,\psi_0,\Delta\psi) = \begin{cases} 0 & \text{if } \psi \le \psi_0 - \Delta\psi \\ \varepsilon_0 & \text{if } \psi \ge \psi_0 + \Delta\psi \\ \varepsilon_0 \left(\frac{1}{2} + \frac{1}{2}\sin\frac{\pi(\psi-\psi_0)}{2\Delta\psi}\right) & \text{if } |\psi-\psi_0| < \Delta\psi \end{cases} \tag{21}$$

  For a smooth function s, we expect the energy in the high modes to decay as $(1/p)^n$ for polynomial order p (we have found that $n \sim 4$ works well in practice). The corresponding value of the sensor is

$$\psi(s) = \log_{10} E_H/E = \log_{10}(1/p)^n = -n \log_{10} p. \tag{22}$$

  We use this value to automate the selection of the parameter ψ_0 in (21), multiplied by a constant of $\mathcal{O}(1)$.

- $F^i(u,q)$ are the fluxes for the model terms (viscous)

In the examples shown here, we use two different stabilization models:

- The eddy viscosity stabilization, with sensor $s^1(u) = \tilde{\nu}$ and a Laplacian model term in the turbulence model equation (7).

- The shock stabilization for transonic problems, with sensor $s^2(u) = \rho$ (density) and Laplacian model terms for each of the equations (1)-(3). In [8], we showed that for strong shocks better results can be obtained by, for example, physical viscosity models, but here we use Laplacian viscosity for simplicity.

We note that our stabilization approach smears the solution so that it can be adequately represented by the grid. In addition, the whole stabilization term is linearized when solving implicitly. This is in contrast to methods based on limiting or filtering (stabilization by reducing the polynomial order or limiting the high frequency components), where the computation of implicit solutions requiring linearization is less straightforward. Furthermore, although our model terms will reduce the overall accuracy of the method, the error introduced decreases with h/p.

C. High-Order Meshes

Generating unstructured meshes for high-order methods is a challenging task, since in general curved mesh elements are required to accurately represent the geometry. For an isotropic mesh it is fairly straight-forward to generate curved elements only adjacent to the curved boundaries, see Fig. 2, left. With a mechanism for placing additional high-order nodes on the curved boundary, the remaining nodes within each element can be relocated to create an accurate and well-conditioned polynomial representation of the element.

For anisotropic boundary layer meshes the situation is more complicated, see Fig. 2, right. Because of the high aspect ratios close to the curved boundaries, several layers of elements have to be curved in order for the elements not to overlap. Generating these meshes in an automatic, unstructured way is still an open research area, in particular in three dimensions.

In this paper, we create meshes using structured grid techniques. By ensuring that the number of elements in each direction is a multiple of the polynomial order p, we can identify the coarse elements from a subset of the nodes and use the remaining nodes to define the high-order element. Note that with this technique all the elements have to be treated as curved during the discretization (even the isotropic ones), but this does not pose any problems in our implementation.

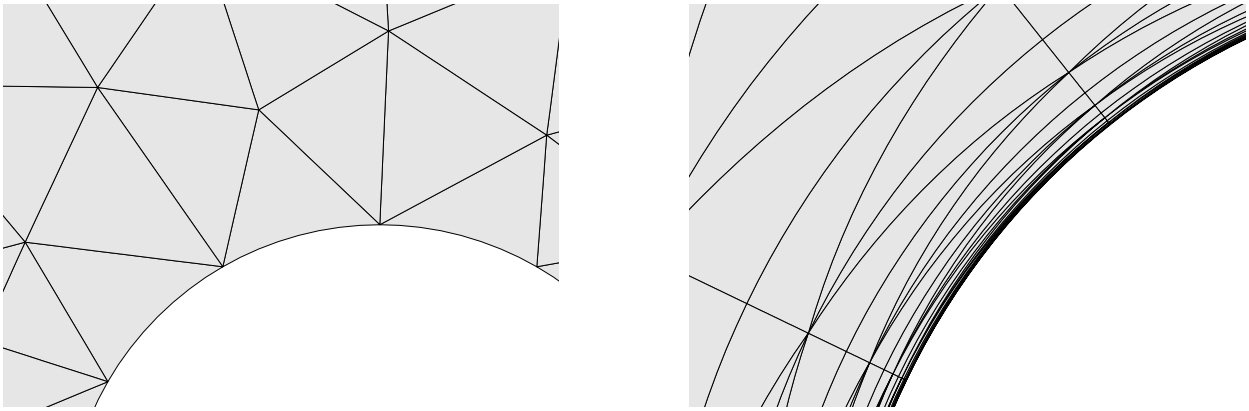

Figure 2. High-order meshes, isotropic (left) and highly anisotropic (right). In the anisotropic case, several layers of elements must be curved in order for the elements not to overlap.

IV. Results

A. Turbulent Flow Past a Flat Plate

We consider the incompressible flow over a smooth flat plate studied experimentally by Wieghardt and included in the 1968 AFOSR-IFP Stanford Conference as a validation case of CFD codes.[5] The free-stream Mach number is set to 0.2 to accelerate the convergence of the compressible flow codes.

For the convergence studies, we use three grids of different resolution. Grid B was obtained by removing every second node in both coordinate directions from grid A, and grid C was similarly obtained from grid B. This technique produces a sequence of grids suitable for convergence study. Grid lines are clustered

around the leading edge of the plate to resolve flow gradients there and around the wall surface to resolve the boundary layer. We note that grid C is extremely coarse. The DG meshes are created from these grids and summarized in Table 1. The last DG mesh in the table is a very fine $p = 4$ mesh, which is used as a reference grid to assess the convergence rates.

Grid	Polynomial order	Resolution	Points on plate	Off-wall spacing	Leading-edge spacing
C	1	10×16	13	1.02×10^{-4}	5.50×10^{-3}
	2	19×31	25	5.10×10^{-5}	2.75×10^{-3}
	3	28×46	37	3.40×10^{-5}	1.83×10^{-3}
	4	37×61	49	2.55×10^{-5}	1.38×10^{-3}
B	1	19×31	25	3.96×10^{-5}	2.38×10^{-3}
	2	37×61	49	1.98×10^{-5}	1.19×10^{-3}
	3	55×91	73	1.32×10^{-5}	7.93×10^{-4}
	4	73×121	97	9.90×10^{-6}	5.95×10^{-4}
A	1	37×61	49	1.76×10^{-5}	1.11×10^{-3}
	2	73×121	97	8.80×10^{-6}	5.55×10^{-4}
	3	109×181	145	5.87×10^{-6}	3.70×10^{-4}
	4	145×241	193	4.40×10^{-6}	2.78×10^{-4}
A0	4	289×481	385	2.07×10^{-6}	1.34×10^{-4}

Table 1. Summary of DG meshes used for the computation.

In all cases, we start with a uniform flow field at free-stream conditions and integrate in time using the implicit backward Euler method with adaptive step size control to find the steady-state solution. The RANS-SA equations, as discretized by CDG, can then be linearized with respect to the previous solution and solved by the Newton's method. The full Jacobians are computed and stored as sparse matrices, and the linear systems are solved using a GMRES solver.

We first present the computed turbulent quantities and compare with the experimental data obtained by Wieghardt[5] and with the law of the wall theory. The near wall behavior of the flow field in terms of the non-dimensional velocity profile $u^+ = u/u_\tau$ versus $y^+ = yu_\tau/\nu$ at $Re_x = 1.02 \times 10^7$ is shown in Figure 3(a) for several polynomial orders and meshes; here $u_\tau = \sqrt{\nu \partial u/\partial y(y=0)}$ is the friction velocity. We see that, the computed velocity profiles match well with the experimental data in the log layer and with the law of the wall for the velocity in the viscous sublayer. Note that the law of the wall for velocity profile takes after the Spalding's formula[14] which has been confirmed by experiment as an excellent fit to inner-law data in the viscous sublayer. Figure 3(b) shows the skin friction distribution over the plate for the same polynomial orders/meshes and for the experimental measurements. The skin friction predictions are in pretty good agreement with the experimental data. We would like to point out that good results are obtained even for pretty coarse DG meshes.

We next investigate the actual impact of our artificial viscosity model term made on the eddy viscosity and the computed turbulent quantities. For this purpose, we present the eddy viscosity distribution in Figure 4(a) and the elements where the applied artificial diffusion is non-zero Figure 4(b). (Recall that the artificial viscosity model term is applied only to the SA equation, *not* to RANS equations.) Note that for plotting purposes the vertical scale has been magnified. We observe that the eddy viscosity transitions very smoothly to the free-stream value and that the applied artificial diffusion is added along the edge of boundary layer without affecting the eddy viscosity in the viscous sublayer and log layer. We thus expect that the introduction of the artificial viscosity model term into the SA equation will not cause deviations from the original SA model without this term. As shown in Figure 5, the velocity profiles obtained with and without introducing the artificial viscosity model term are indeed very similar. It is also important to note that the SA equation without the stabilizing term produces a non-smooth transition along the edge of

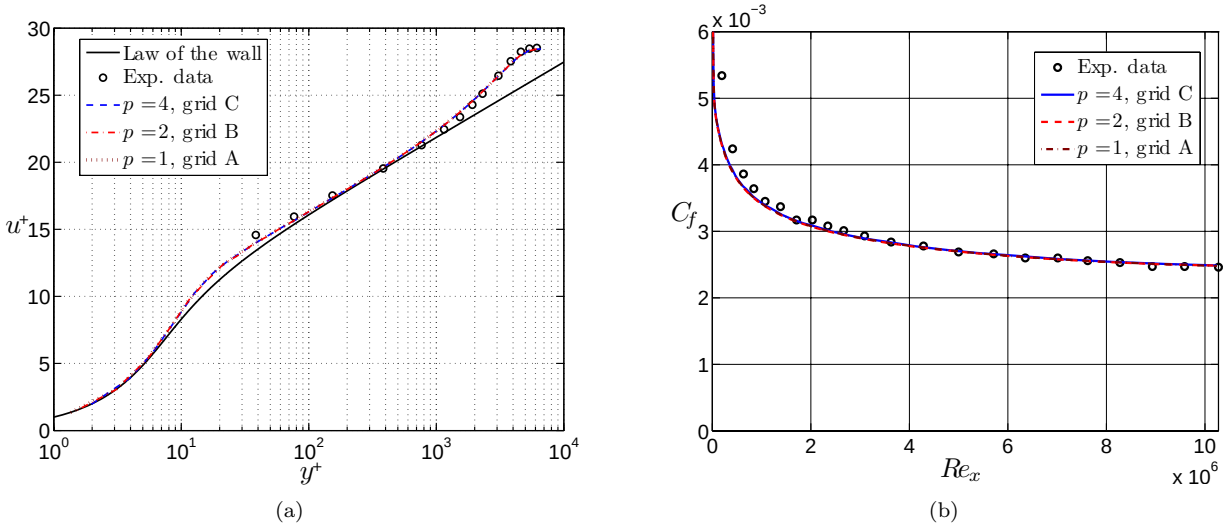

(a) (b)

Figure 3. Comparison between the computed turbulent quantities and the experimental data in a flat-plate boundary layer: (a) velocity profiles at $Re_x = 1.02 \times 10^7$ and (b) skin friction coefficient as function of Re_x.

boundary layer for the eddy viscosity. For reasonably fine meshes, computing solutions is still possible but for coarse grids such as ones constructed from grid C we are unable to obtain converged solutions.

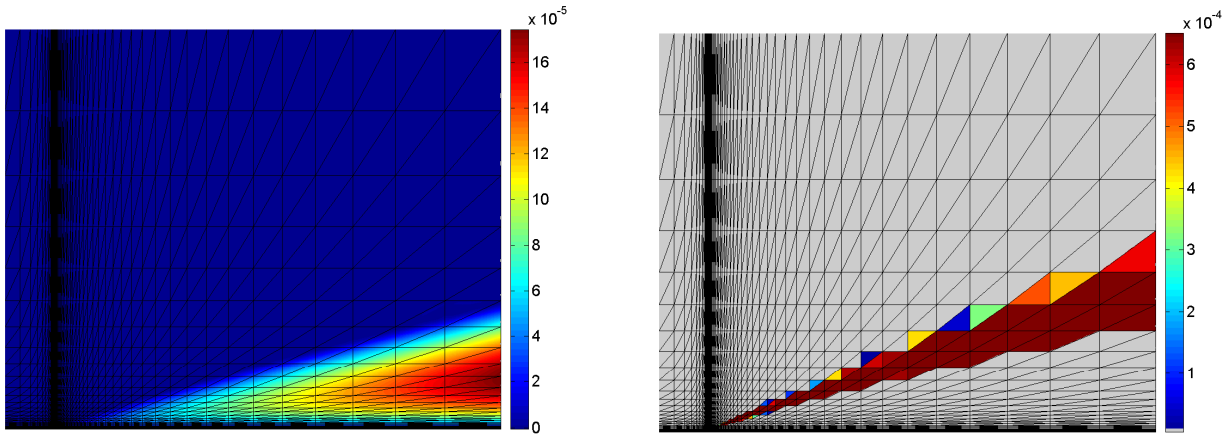

(a) (b)

Figure 4. The left plot show the eddy viscosity for a flat plate with interpolation of degree $p = 4$ on grid A. The right plot shows the applied diffusion. Note how the artificial diffusion is added along the edge of boundary layer so that the eddy viscosity transitions smoothly to free-stream value there.

Finally, we present grid refinement results. We show in Table 2 the error in drag and the spatial convergence rates for several orders of approximations and DG meshes given in Table 1. Here, the total drag coefficient obtained with the last DG mesh in Table 1 is used as the reference value. (Because of the flow singularity at the leading edge, the value of total drag on the entire plate obtained on different meshes is not a good to estimate the convergence rates. To eliminate this singularity error, the total drag was estimated over a section of the flat plate only ($0.0148 \leq x \leq 4.687$).) The error in drag decreases rapidly with increasing p and decreasing h. The order of accuracy $O(p)$ for a derivative quantity such as drag is the expected optimal order of convergence. The advantage of using high-order approximations is clearly observed: for example, the $p = 4$ solution on grid C is more accurate than the $p = 1$ solution on grid A as shown in Table 1 and in fact also considerably less expensive. The higher-order approximations thus produce far more accurate solutions on relatively coarse grids and thereby lead to reduction in both storage requirements and

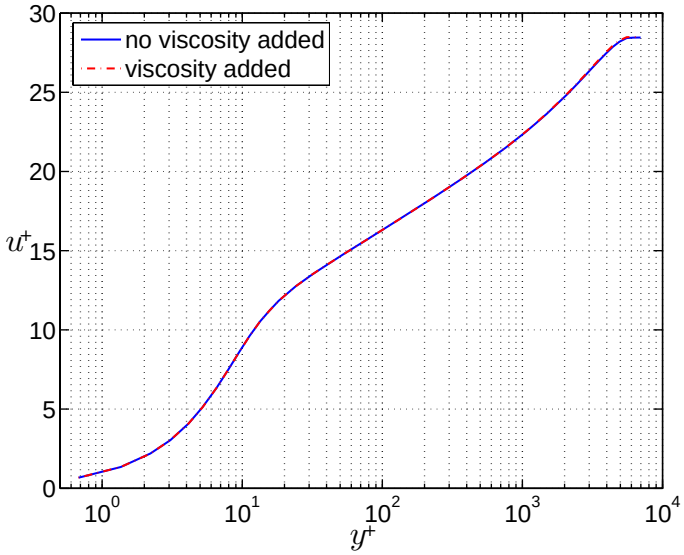

Figure 5. Comparison of the velocity profiles obtained with the S-A one-equation model with and without the artificial viscosity model term for $p = 2$ on the grid B. Note the velocity profiles are very similar.

computational time.

Grid	A		B		C	
p	Error	Rate	Error	Rate	Error	Rate
1	1.2919×10^{-5}	1.03	2.6325×10^{-5}	1.03	5.3899×10^{-5}	—
2	1.1136×10^{-6}	2.07	4.6556×10^{-6}	2.15	2.0639×10^{-5}	—
3	1.5429×10^{-7}	3.31	1.5347×10^{-6}	3.08	1.3002×10^{-5}	—
4	1.6431×10^{-8}	4.54	3.8321×10^{-7}	4.06	6.3715×10^{-6}	—

Table 2. Errors in drag and convergence rates for the turbulent flow past a flat plate.

B. Turbulent Flow Past a NACA 0012 Airfoil

We also present results for a turbulent flow past NACA 0012 airfoil at both subsonic and transonic speeds. In both cases, we use a single-block, two-dimensional C-grid of 101 x 31 nodes. The grid is clustered around the leading edge and the trailing edge and around the airfoil surface to resolve the boundary layer on the airfoil. The first grid point off the wall is at a distance of 2.82×10^{-5} from the airfoil surface. Our DG meshes constructed from this grid have the resolution scaled up with the polynomial order.

We first consider the subsonic case at free-stream Mach number $M_\infty = 0.3$, Reynolds number of 1.85×10^6, and zero angle-of-attack for which the experimental data is available in [1]. We present in Figure 7 the pressure coefficient distribution for polynomial orders of $p = 2$, $p = 3$ and $p = 4$. (Note the steady-state solutions are obtained from time-marching uniform flow fields at free-stream conditions by using the implicit backward Euler scheme and the Newton's method.) We see that numerical predictions agree quite well with the experimental measurements. The close-up near the leading edge shows oscillations in the pressure associated with the low order ($p = 2$) solution. Figure 8 shows the contour plot of Mach number associated with the $p = 4$ solution. Finally, we show in Figure 9 the eddy viscosity distribution and the elements where the artificial viscosity model term is non-zero. Again, we observe a smooth transition of the eddy viscosity to its free-stream value.

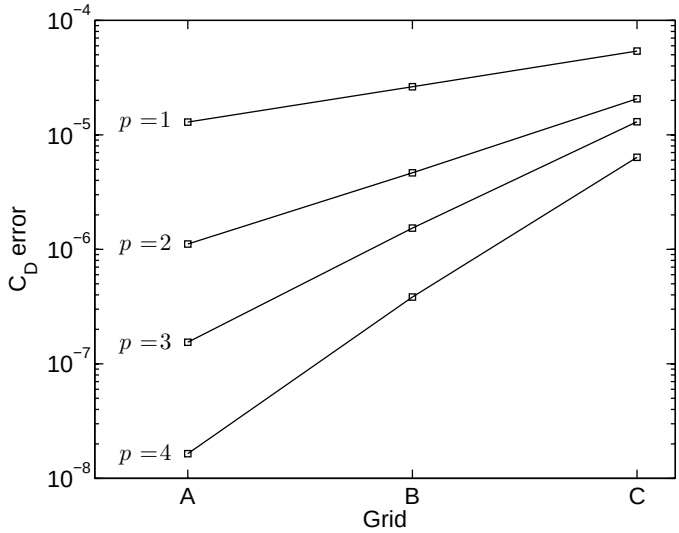

Figure 6. Errors in drag for the turbulent flow past a flat plate, see Table 2 for detailed values and convergence rates.

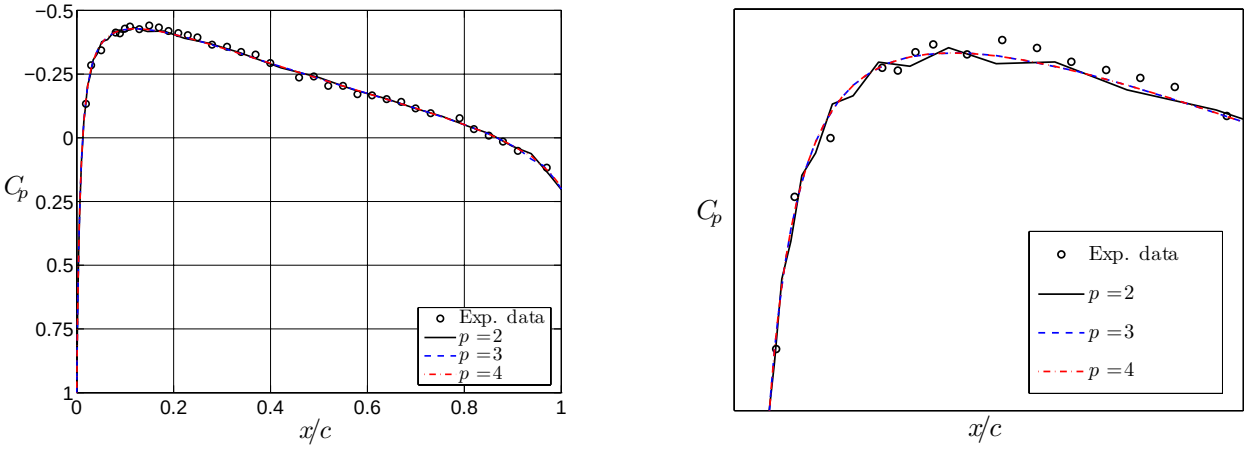

Figure 7. Pressure coefficient distribution (left) over the upper airfoil surface for the subsonic turbulent flow past a NACA 0012 foil at Mach 0.3 and $\alpha = 0$. The close-up near the leading edge (right) exhibits oscillations in the pressure for $p = 2$ solution.

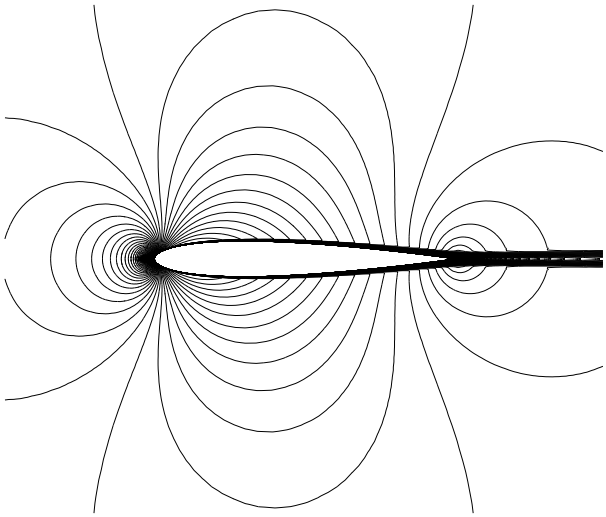

Figure 8. Contour plot of Mach number for the $p = 4$ solution for the subsonic turbulent flow past a NACA 0012 foil at Mach 0.3 and $\alpha = 0$.

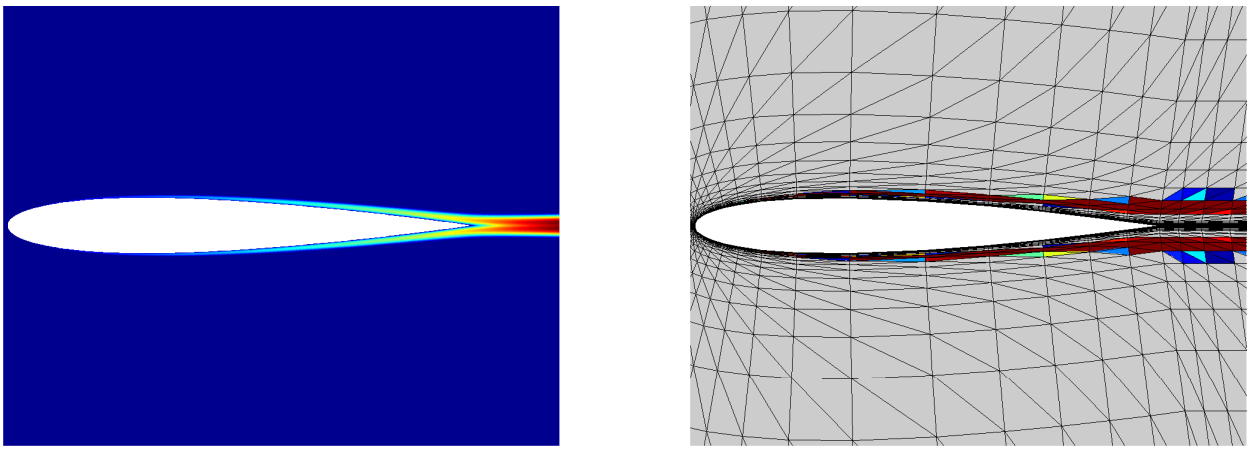

Figure 9. Eddy viscosity (left) and diffusion applied to it (right) for the $p = 4$ solution for the subsonic turbulent flow past a NACA 0012 foil at Mach 0.3 and $\alpha = 0$. Note that diffusion is only applied at the edge of the boundary layer with the gray color indicating that no diffusion is added.

Next we consider a transonic turbulent flow on a NACA0012 airfoil at free-stream Mach number $M_\infty = 0.85$, Reynolds number of 1.85×10^6, and zero angle-of-attack. Here, in addition to the artificial viscosity model term for the eddy viscosity, we need to consider shock capturing artificial viscosity. We add a Laplacian model terms to each of the RANS equations: the element-wise shock indicator is based on the components of the Koornwinder decomposition of the density, and equal amounts of viscosity are added to all the RANS equations. Figure 10 shows the steady-state $p = 4$ solution (Mach number) and artificial diffusion added to the RANS equations. Our shock indicator identifies the elements around the shock, and no viscosity is added to the elements further away. Hence, the shock is sharp and well-resolved within only one element. In Figure 12, Mach number plots for both $p = 3$ and $p = 4$ solutions show that the shock is sharper with higher-order approximations. We furthermore present in Figure 13 the pressure distribution and skin-friction distribution over the upper airfoil surface. We note that that for $p = 3$ and $p = 4$ both the pressure and skin friction coefficients are essentially grid independent, whereas for the $p = 2$ significant differences are observed in skin friction.

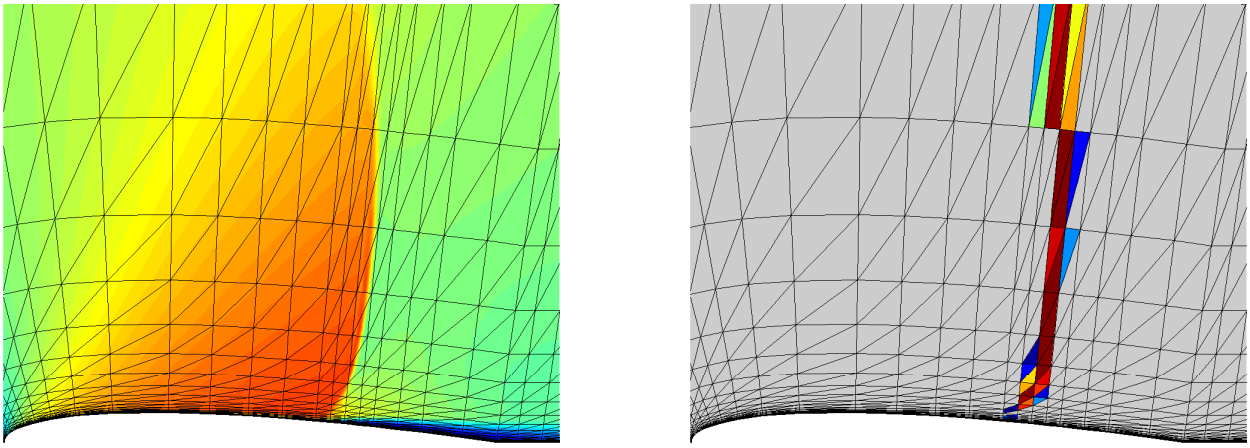

Figure 10. Mach number (left) and shock diffusion applied to the RANS equations (right) for transonic turbulent flows past a NACA airfoil at Mach 0.85 with polynomial order $p = 4$. Note that, the shock is well resolved within one element and that artificial diffusion is added only in the shock region, with the gray color representing no diffusion added.

C. Turbulent Flow Past a 2D Cylinder

Finally, we present unsteady RANS (URANS) and Detached Eddy Simulations (DES)[12] solutions for turbulent flow past a 2D cylinder of unity diameter. The DES computations are carried out essentially with the same equations but with a modified wall distance function d in the destruction term of the turbulent equations 7. We caution that 2D DES results are probably not justified form a physical standpoint, and only shown a numerical experiment to indicate the direction in our future research. The flow is calculated with turbulent separation at Reynolds number 3×10^6 and Mach number 0.2. The DG mesh is of O-type grid with 18,432 $p = 2$ elements, 20 cylinder diameters long, and off-wall spacing 3.8×10^{-6}. The time integration is carried out implicitly with time step $\Delta t = 0.02$ seconds.

We present the Mach number behind the cylinder for the URANS solution in Figure 14(a) and DES solution in Figure 14(b). We notice that URANS and DES produce solutions with significantly different structures: the vortex shedding is suppressed by the smoothing effect of the RANS model, while being preserved by DES computations. The pressure distributions C_p and skin-friction distributions C_f are shown in Figure 15(a) and 15(b), respectively. In the URANS case, the separation occurs at angle $\theta_{\text{sep}} = 111^o$ which is in excellent agreement with the computed value of 111^o obtained with the TS7 case reported in [12].

V. Conclusions

We have presented a practical approach to RANS solutions using high-order DG approximations. We believe that this is an important ingredient to making higher-order methods viable in important research

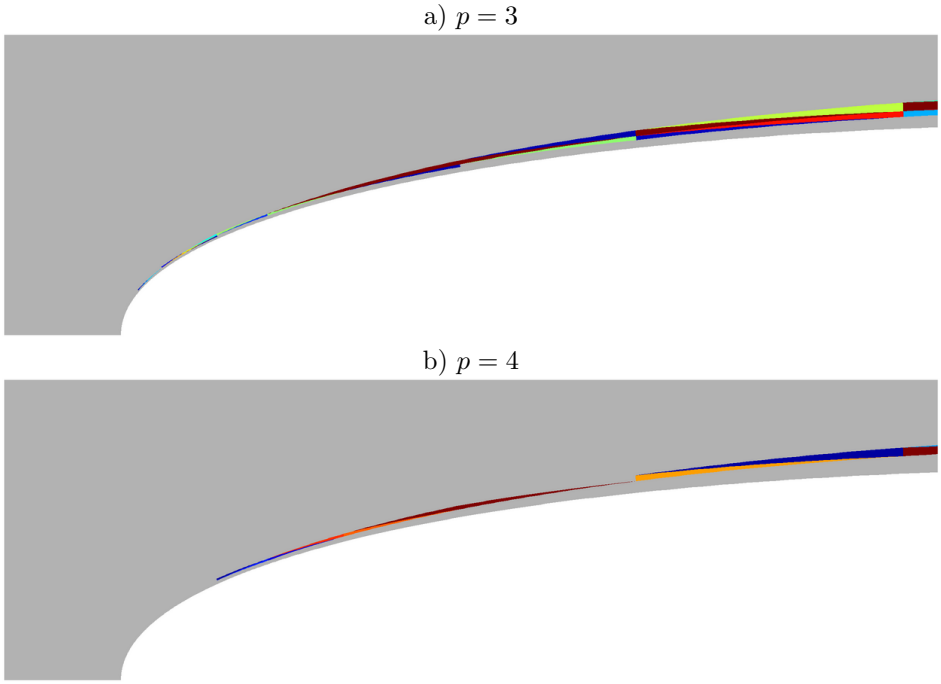

Figure 11. Artificial diffusion applied to the turbulence equation for the flows past a NACA airfoil at Mach 0.85 with polynomial order $p = 3$ (top) and $p = 4$ (bottom). Note that viscosity is only added at the edge of the boundary layer to smear out the eddy viscosity profile. Note also that the overall effect of this artificial viscosity on the solution can not be observed from the C_p and C_f plots.

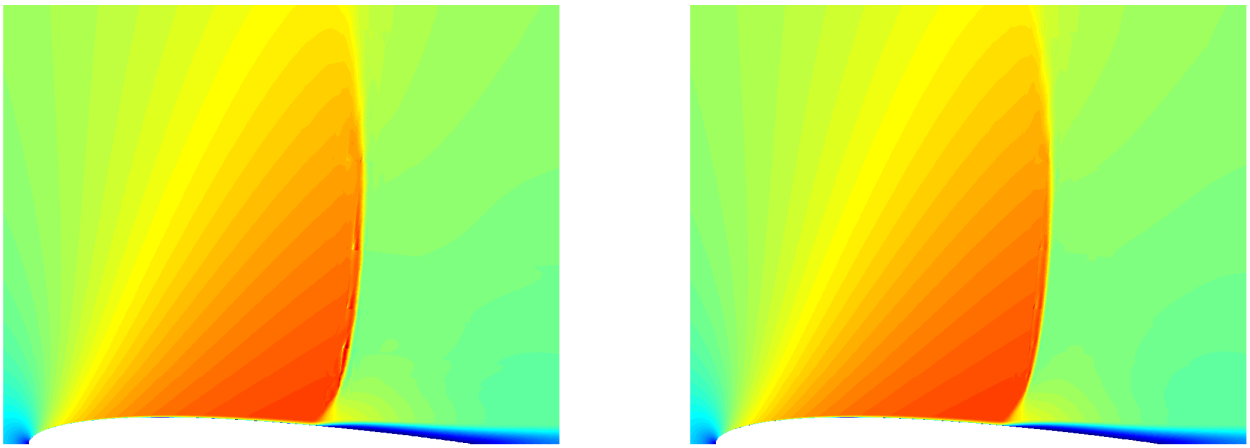

Figure 12. Mach number for $p = 3$ solution (left) and $p = 4$ solution (right) for transonic turbulent flows past a NACA airfoil at Mach 0.85 and $\alpha = 0$. Note how the shock is well-resolved with using higher polynomial order.

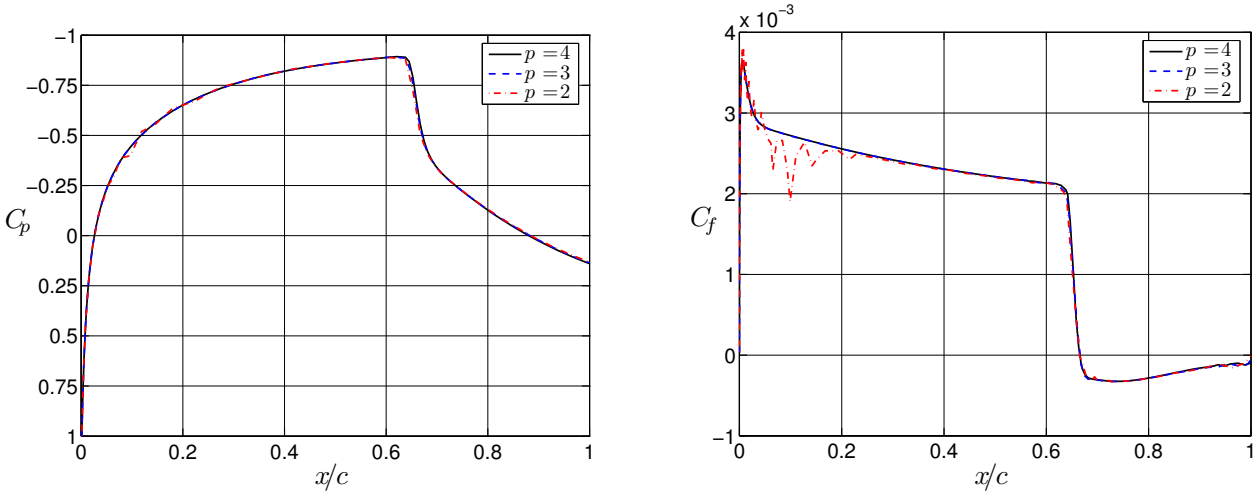

Figure 13. The pressure coefficient (left) and skin-friction coefficient (right) over the upper airfoil surface for the transonic turbulent flow past a NACA 0012 foil at Mach 0.85 **and** $\alpha = 0$**.**

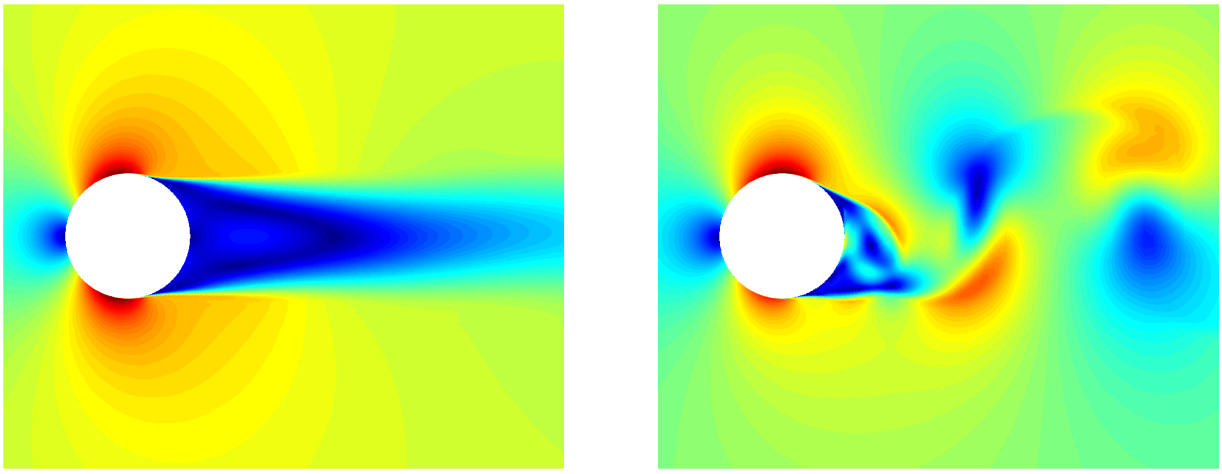

(a) (b)

Figure 14. Comparison between URANS and DES solutions for turbulent flow past a 2D cylinder at $Re_D = 3 \times 10^6$**: (a) Mach number for the RANS solution and (b) Mach number for DES solution. Note that URANS smears out the solution, while DES creates the vortex shedding behind the cylinder.**

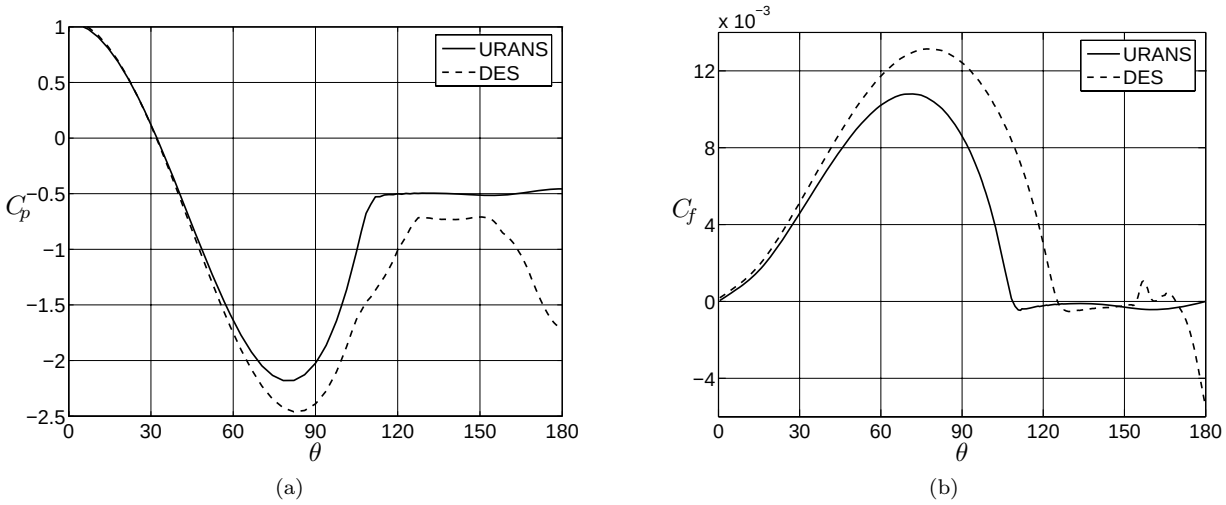

Figure 15. Comparison between URANS and DES results for turbulent flow past a 2D cylinder at $Re_D = 3\times10^6$: (a) pressure coefficient and (b) skin-friction coefficient.

applications. In this paper, high-order DG solutions (in the range $p = 2 - 4$) of the RANS equations for a number of turbulent flows have been obtained. Numerical results have been validated with the available experimental measurements. A grid convergence study has been used to demonstrate that the higher-order approximations produce far more accurate solutions on a given mesh resolution, thereby offering the potential for substantial reductions in computational time. This result is a combination of the CDG method and the artificial viscosity treatment of the eddy viscosity in the SA turbulence model. It has been shown that the artificial viscosity model term is only active at the edge of boundary layer and shear layer, thus having a very minor effect on the overall solution. Our current research effort is directed at the implementation of this approach for Detached Eddy Simulation of complex turbulent flows in three dimensions. In this paper we have only considered structured-like discretizations, but it is clear that one of the main advantages of DG methods is the ability to handle complex geometries. This will be the focus of our future research.

VI. Acknowledgments

The authors would like to thank the Singapore-MIT Alliance for the partial support of this work and Mark Drela from MIT for many helpful discussions.

References

[1]AGARD, *Experimental Data Base for Computer Program Assessment*, Report of the Fluid Dynamics Panel Working Group 04, AGARD-AR-138, May 1979.

[2]Bassi, F., and Rebay, S., *A high-order accurate discontinuous finite element method for the numerical solution of the compressible Navier-Stokes equations*, J. Comput. Phys., 131 (1997), pp. 267279.

[3]Bassi, F., Crivellini, A., Rebay, S., and Savini, M., *Discontinuous Galerkin solution of the Reynolds-averaged NavierStokes and $k-\omega$ turbulence model equations*, Computers & Fluids, Vol. 34, No. 4-5, 2005, pp. 507–540.

[4]Cockburn, B., and Shu, C.-W., *The local discontinuous Galerkin method for time-dependent convection-diffusion systems*, SIAM J. Numer. Anal., Vol. 35, No. 6, 1998, pp. 2440-2463.

[5]Coles, D.E., and Hirst, E.A., *Computation of Turbulent Boundary Layers*, AFOSR-IFP-Stanford Conference, Vol. II, Stanford University, CA, 1969.

[6]Koornwinder, T. H., *Askey-Wilson polynomials for root systems of type BC*, Hypergeometric functions on domains of positivity, Jack polynomials, and applications (Tampa, FL, 1991), Vol. 138 of Contemp. Math., Amer. Math. Soc., Providence, RI, 1992, pp. 189204.

[7]Peraire, J., and Persson, P.-O., *A compact discontinuous Galerkin (CDG) method for elliptic problems*, submitted to SIAM Journal for Numerical Analysis, 2006.

[8]Persson, P.-O., and Peraire, J., *Sub-Cell Shock Capturing for Discontinuous Galerkin Methods*, AIAA-2006-0112, Reno, January 2006.

[9]Persson, P.-O., and Peraire, J., *An Efficient Low Memory Implicit Discontinuous Galerkin Algorithm for Time Dependent*

Problems, AIAA-2006-0113, Reno, January 2006.

[10], Roe, P. L., *Approximate Riemann solvers, parameter vectors, and difference schemes*, J. Comput. Phys., 43, 1981.

[11]Spalart, P.R., and Allmaras, S.R., *A one-equation turbulence model for aerodynamic flows*, La Rech. Aérospatiale 1 (1994) 5–21.

[12]Travin, A., Shur, M., Strelets, M., and Spalart, P., *Detached-Eddy Simulations Past a Circular Cylinder*, Int. J. Flow, Turbulence and Combustion, 63, 1999, pp. 293313.

[13]Wilcox, D.C., *Turbulence Modeling for CFD*, 2nd Edition, DCW Industries, Inc., 1998.

[14]White, F.M., *Viscous Fluid Flow*, 2nd Edition, McGraw-Hill, New York, 1991.